Unveiling the acetone sensing mechanism by WO$_3$ chemiresistors through a joint theory-experiment approach

Stefano Americo [a,1], Eleonora Pargoletti [a,b,*], Raffaella Soave [c], Fausto Cargnoni [c], Mario Italo Trioni [c,*], Gian Luca Chiarello [a], Giuseppina Cerrato [d], Giuseppe Cappelletti [a,b]

[a] *Dipartimento di Chimica, Università degli Studi di Milano, via Golgi 19, Milano 20133, Italy*
[b] *Consorzio Interuniversitario per la Scienza e Tecnologia dei Materiali (INSTM), Via Giusti 9, Firenze 50121, Italy*
[c] *National Research Council of Italy, Institute of Chemical Science and Technologies "Giulio Natta", via Golgi 19, Milano 20133, Italy*
[d] *Dipartimento di Chimica & NIS, Università degli Studi di Torino, via P. Giuria 7, Torino 10125, Italy*

ABSTRACT

The acetone sensing mechanism by WO$_3$ was investigated through a combined experimental and theoretical approach. The $\gamma-$monoclinic WO$_3$ powder was synthesized by a template-mediated sol-gel method and characterized on structural, surface, morphological and optical points of view. A thin film of WO$_3$ was deposited on interdigitated Au electrodes by hot-spray method and tested at 300 °C (while applying a bias of 1.0 V) for acetone gas sensing, both in presence and absence of oxygen in the gas carrier. Interestingly, the absence of oxygen had no significant effect on the sensor response intensity but it dramatically increased the recovery times (from 120 s to 2700 s). In order to explain these experimental results, by means of *ab initio* density functional theory calculations, we modeled a defective $\gamma-$WO$_3$ surface structure and simulated the adsorption of acetone and oxygen molecules on top of it. We unprecedentedly evidenced that, in presence of surface oxygen vacancies, both acetone adsorption and its oxidation reaction can occur. However, their contribution to the sensor response strictly depends on the inert/oxidative atmosphere present in the sensing chamber, which in turn strongly affects the surface oxygen population. Our findings can either be the guidelines for future studies aimed at delineating the possible reaction products or pave the way for the engineering of tailored nanomaterials having specific surface features and enhanced sensing properties.

© 2020 Elsevier Ltd. All rights reserved.

1. Introduction

Diabetes is a lifelong condition that severely affects the quality of life of a rapidly growing number of individuals. The disease is accompanied by a series of metabolic disorders that have to be constantly monitored before reaching dangerous extents, eventually leading to death [1–3]. Acetone has been taken into consideration as a selective bio-marker for type-1 diabetes [4–6], since its concentration in breath can be correlated to insulin and glucose blood levels [7]. This concentration can increase from 300-900 ppb for healthy individuals to 1800 ppb and more in diabetic patients

[8]. Breath analysis by means of portable devices constitutes a valid alternative with respect to traditional techniques, allowing very rapid and non-invasive measurements [4,9,10]. However, in order to detect this small difference (around 900 ppb) between healthy and ill people, in such a complex gas mixture as the human's breath, a highly sensitive and selective acetone sensor is required. Among the various, largely investigated metal oxide-based chemiresistors, SnO$_2$, TiO$_2$, ZnO, In$_2$O$_3$ and WO$_3$ have been widely exploited [11–13]. In particular, tungsten trioxide has proved to be one of the most promising materials for this application, due to its high sensitivity towards Volatile Organic Compounds (VOCs) combined with impressive structural and thermal stabilities [10,14].

If on one hand the technological applications of this material are nowadays well-established, the mechanism that produces, at the atomic level, the final sensor response towards acetone molecules and VOCs in general is still debated [15–18]. Several experimental and theoretical studies have been made on a wide

range of materials and polymorphs, including hexagonal WO_3, SnO_2, ZnO and many more [17,19–23], resulting in very few mechanisms that can be easily generalized to all sensors based on metal oxide materials [15]. The most popular one, known as "ionosorption model", involves either a reception or a transduction step [15,16,24]. Notably, this mechanism is quite close to the one already reported for photodection processes [25,26]. The adsorbed oxygen species can be considered as free oxygen ions electrostatically stabilized on the metal oxide semiconductor (MOS) surface. The first step implies a physisorption mechanism that turns into ionosorption upon electrons transfer from the semiconductor to the oxygen species themselves. Hence, several negatively charged species are formed, such as O_2^-, O^- and O^{2-}. Zheng et al. [27] reported that, in general, below 150 °C, the O_2^- molecular form dominates whereas, above this temperature, the other two atomic species prevail. The chemisorption of these oxygen-containing ions causes the formation of a depleted region, characterized by reduced electron mobility near the MOS surface [15,28]. In the presence of a reducing gas such as acetone or ethanol, the oxygen ions concentration on the MOS surface decreases due to reactions with the target analyte, leading to a larger mobility which results in a current increase. This hypothesis has shown promising results when applied to simple inorganic species such as NO, NO_2 and CO [19,20,29,30], since their reaction mechanism can be explained in terms of single oxygen atom transfer from or towards the surface. However, extending such mechanism to larger organic molecules such as acetone, toluene and ethanol, is a more challenging task, since a complex, multistep reaction would be involved [22,31,32]. Other studies suggest a less popular mechanism, called the "oxygen-vacancy model" [15], which has been recently corroborated also by operando DRIFT spectroscopy adopting tungsten oxide as chemiresistor [33]. As the name implies, this mechanism contemplates the partial reduction and re-oxidation of the MOS surface. Specifically, considering an *n*-type semiconductor, which is rich in oxygen vacancies, its partial reduction upon interaction with a reducing analyte (e.g. ethanol or acetone) can cause the formation of other oxygen vacancies and, consequently, an injection of electrons into the conduction band (CB) of the MOS, thereby increasing the conductivity. Once the analyte is oxidized, it leaves the oxide surface, re-oxidizing it if oxygen, that fills the vacancies, is present in the atmosphere over the material surface [15,17]. A third mechanism has been proposed by Abokifa et al. [17], in which the direct adsorption of VOCs on the MO surface rather than their oxidation by means of ionosorbed oxygen species can explain the sensing performance.

In this work, the combination of experimental and theoretical approaches was exploited in order to possibly unravel the gas sensing mechanism by WO_3 as MOS prototype. WO_3 powder was synthesized through a novel synthetic route comprising the use of a non-ionic surfactant, namely Pluronic® F127, in order to smoothly increase the final active surface area, which is known to play a pivotal role in the sensing behavior [3,34]. Sensing tests were performed at high operating temperature (300 °C) in simulated air, evidencing very promising features of the as-prepared material in terms of either sensitivity or response/recovery times. Moreover, to give insights into the role played by the oxygen species, the same tests were carried out in inert N_2 atmosphere. In parallel, density functional theory (DFT) [35] was exploited in order to better elucidate the sensing mechanism. Therefore, after defining the WO_3 bulk and surface structures, the adsorption of the in-play gaseous species, such as acetone and oxygen, was simulated. Our results unprecedentedly highlight that, alongside the key role of gaseous O_2 in forming negatively adsorbed species and reacting with the analyte molecules, also the direct acetone adsorption onto the WO_3 surface should be considered in order to explain the sensor response.

2. Experimental

2.1. Synthesis of WO_3 nanopowder

All the chemicals were of reagent-grade purity and were used without further purification; doubly distilled water passed through a MilliQ apparatus was utilized. All the reagents used were purchased from Sigma-Aldrich.

In a typical synthesis, 2.0 g of Pluronic® F127 (as templating agent) were dispersed in a mixture of ethanol (25 mL) and MilliQ water (20 mL). Under vigorous stirring (at 80 °C), ca. 5.0 g of H_2WO_4 (templating agent/tungsten precursor weight ratio equal to 0.4) were added into the previous ethanol/aqueous solution. The system was kept under stirring at 200 rpm for 3 h. The resultant sol solution was dried in oven at 60 °C, then calcined at 400 °C under oxygen flux (5 h, 9 NL h^{-1}) to remove the organic traces. Finally, the powder was washed several times with ethanol and MilliQ water to eliminate the residual block copolymers. Afterwards, the as-synthesized powder was dried in oven at 60 °C.

2.2. Physico-chemical characterizations

X-ray diffraction (XRD) analyses were performed on a Philips PW 3710 Bragg-Brentano goniometer equipped with a scintillation counter, 1° divergence slit, 0.2 mm receiving slit and 0.04° soller slit systems. We employed graphite-monochromated Cu Kα radiation (Cu Kα_1 λ = 1.54056 Å, Kα_2 λ = 1.54433 Å) at 40 kV × 40 mA nominal X-rays power. Diffraction patterns were collected between 10° and 70° with a step size of 0.02° and a total counting time of about 1 h. A microcrystalline Si-powdered sample was used as a reference to correct for instrumental line broadening effects.

The morphology was investigated by high-resolution transmission electron microscopy (HR-TEM) using a JEOL JEM 3010UHR microscope operating at 300 kV and equipped with a LaB$_6$ single crystal filament. Sample powders were dry deposited on 200 mesh Cu "holey" carbon grids before the analyses.

Specific surface area and porosity distribution were determined from N_2 adsorption/desorption isotherms at 77 K using a Micromeritics Tristar II 3020 (Norcross, USA) apparatus and the instrumental software (Version 1.03) by applying Brunauer-Emmett-Teller (BET) and Barrett-Joyner-Halenda (BJH) analyses, respectively. Before measurements, sample powders were pretreated at 150 °C (4 h under N_2 flux) to remove adsorbed species.

In order to evaluate powders optical band gaps by Kubelka-Munk elaboration, diffuse reflectance spectra (DRS) were measured on a UV/Vis spectrophotometer Shimadzu UV-2600 equipped with an integrating sphere; a "total white" $BaSO_4$ was used as reference.

2.3. Deposition of WO_3 onto interdigitated electrode

WO_3 powder was deposited on alumina substrates topped with interdigitated Au electrodes (IDEs) by hot-spray method. The IDEs were made of alumina on which interdigitated Au lines with 200 μm in width and space have been deposited (G-IDEAU200, DropSens, Oviedo, Spain) [25]. To remove any contamination from the electrodes, all substrates were sintered at 300 °C for 6 h and washed by several washing ethanol/drying cycles before deposition. Then, 4.0 mL of 2.5 mg mL^{-1} ethanol powders suspensions were sprayed by keeping constant the air-brush pressure (0.8 bar), the temperature of the heating plate (230 °C) and the deposition height (ca. 8 cm). A final calcination step at 350 °C for 1 h was performed to guarantee a good powders film adhesion on the IDE.

2.4. Sensing tests

Sensing tests were performed using a custom-built stainless steel cell [36]. The IDE coated sensors were placed above a hotplate connected to a PID (Proportional-Integral-Derivative) temperature controller, and the upper part of the cell was closed with a quartz window. The sensor response was measured while flowing either a 80% N_2 – 20% O_2 gas mixture or 100% N_2 (in both cases 0.5 L min^{-1} was set as the total flow rate) regulated by mass flow controllers (Bronkhorst, The Netherlands). The desired amount of target gases up to 20 ppm was introduced into the cell by means of a four-way switching valve. The analyte concentration was varied by dilution of a proper flow of a starting 500 ppm acetone in N_2 gas mixture, keeping constant the total flow rate of 0.5 L min^{-1}. For the gas sensing tests, two gold probes were separately placed on top of the powders covered IDE and the dynamic response was recorded by an electrochemical workstation (Autolab PGStat30, Ecochemie, The Netherlands, potentiostat/galvanostat controlled by NOVA 2.0 software), applying a bias of +1.0 V. Tests were performed at very low water content (RH less than 2%) and at different temperatures (in the range 150-350 °C) to assess the optimal one. Indeed, the aim was not to unravel the role played by water but only the VOCs sensing mechanism. As already stated [37,38], an increase of RH percentage leads to a drastic reduction of the sensor response. The sensor response is reported as (R_{air} / $R_{analyte}$)−1, where R_{air} is the film resistance in air and $R_{analyte}$ is the film resistance at a given concentration of the target gas which varies with time [39,40]. Both sensors response and recovery times have been evaluated considering the 90% of the final response, as already reported elsewhere [39,40].

3. Computational details

Ab-initio calculations on $\gamma-$monoclinic phase of WO_3 [41,42] were performed using DFT as implemented in the SIESTA code (Spanish Initiative for Electronic Simulation with Thousands of Atoms) [43], choosing PBE [44] as the exchange-correlation functional. Norm-conserving pseudopotentials for W and O were generated, based on the Troullier-Martins parameterization [45]. The tungsten pseudopotential includes scalar relativistic corrections and was generated for the $[Xe]4f^{14}6s^15d^5$ configuration, utilizing the cutoff radii provided by Rivero et al. [46]. The basis set for tungsten is of DZP type and has been taken, without modifications, from the same authors [46]. For oxygen atoms we have uniformly used a value of 1.47 Å for the radii of all the angular components of the pesudopotential, while the basis set was a custom DZP which included the cutoff radii suggested by Lambert-Mauriat et al. [47], further corrected by changing the second cutoff radius of the 2s basis functions from 5.2 Å to 2.2 Å.

Bulk phase calculations were performed on a $6 \times 6 \times 6$ k-point grid in the 32 atoms monoclinic unit cell, with **b** as unique axis, using a 450 Ry as mesh cutoff. In order to overcome the heavy band gap underestimation typical of pure functionals such as PBE, we applied to the oxygen pseudopotential the half-occupation technique described by Ferreira et al. [48,49], which led to great improvements in the band gap value. After the treatment, the latter increased from 1.1 eV to 2.48 eV, which is much closer to the experimental gap (2.6 - 2.7 eV) reported in literature [50–52] and measured by ourselves (see Section 4.1).

4. Results

4.1. WO₃ material characterization

The structural properties of the as-synthesized WO_3 nano-powder were first investigated by XRD analysis. Figure 1(a)

displays the registered X-ray pattern, in which the characteristic peaks at 2θ = 23.1°, 23.7° and 24.3° correspond to the (0 0 2), (0 2 0) and (2 0 0) Miller's indexes of the monoclinic polymorph. Moreover, the XRD line reveals a good degree of sample crystallinity, as witnessed by the crystallite domains size of 30 nm.

Surface morphological properties were evaluated through N_2 adsorption/ desorption analysis. The specific surface area value is quite low (7 m^{2}g^{-1}) as expected for WO_3-based materials [53,54], as well as the total pore volume of 0.030 cm^{3}g^{-1} (as shown in inset of Fig. 1b). Notably, both the presence of F127 tenside and the calcination step may have contributed to the high percentage of macropores, with diameters greater than 20 nm (inset of Fig. 1b). Furthermore, the BET hysteresis loop, reported in Fig. 1(b), indicates the presence of typical H3-type pores, *i.e.* slit-shaped ones.

On the morphological point of view, high-resolution TEM images, in Fig. 1(c), display highly crystalline particles that form dense aggregates having micrometric and sub-micrometric sizes. Specifically, the analysis of both the interference fringes (observable in the magnification of the HR-TEM image in Fig. 1c) and the Fourier Transform pattern (inset) evidence the presence of monoclinic WO_3 (ICDD n. 01-075-2072) [55], with spacing between planes ascribable to d(1 1 1) of 0.31 nm.

Finally, as regards the optical properties, band gap values were determined by Kubelka-Munk elaboration of the relative diffuse reflectance spectrum (Fig. 1d) resulting in an optical band gap of 2.6 eV, a value comparable to those already reported for tungsten trioxide [50–52].

4.2. Chemical sensing properties

The performance of the as-prepared material was investigated at the optimal temperature of 300 °C Fig. 2(a) in simulated air, *i.e.* 80% N_2 – 20% O_2, mimicking the major carrier of the humans breath. The relative response obtained is displayed in Fig. 2(b) (black line). Remarkably, 200 ppb could be easily detected showing a quite fast response of about 70 s and a recovery time of ca. 120 s, values comparable to the most performing WO_3-based sensors already reported in literature [1,6,56].

Alongside with the achievement of a highly sensitive WO_3 sensor, our final aim is to provide a comprehensive description of the sensing mechanism by MOS nano-architectures. In order to do so, perceiving the role of oxygen in either enhancing or quenching the MOS sensing features is crucial. Experimentally, this aspect was investigated by performing an additional test in inert atmosphere (100% N_2), shown in Fig. 2b (red line). Interestingly, an intense signal, comparable with the one measured in the previous test, was observed independently of the presence of gaseous O_2. In this case, however, both the response and recovery times were higher and, especially, the latter were affected by a dramatic increase (from 120 s to 2700 s). Finally, we performed a hybrid test (see Fig. 2d) where the response to 20 ppm acetone was measured, at first, under 100% N_2 flow; then, in recovery phase, the atmosphere composition was changed to simulated air. Finally, another peak at 20 ppm acetone was measured under these conditions. This test highlights the differences in the raw current output according to the composition of the gaseous environment. In particular, in inert atmosphere the current intensity is generally higher with respect to the test performed in presence of O_2. In order to retrieve useful information concerning the sensing mechanism, the experimental data described in this section were combined with the theoretical ones. Therefore, the following theoretical simulations were conducted: *i*) bulk and surface structure of the $\gamma-$monoclinic WO_3 material, in stoichiometric form as well as in presence of oxygen vacancies; *ii*) adsorption of acetone and oxygen species on the defective surface.
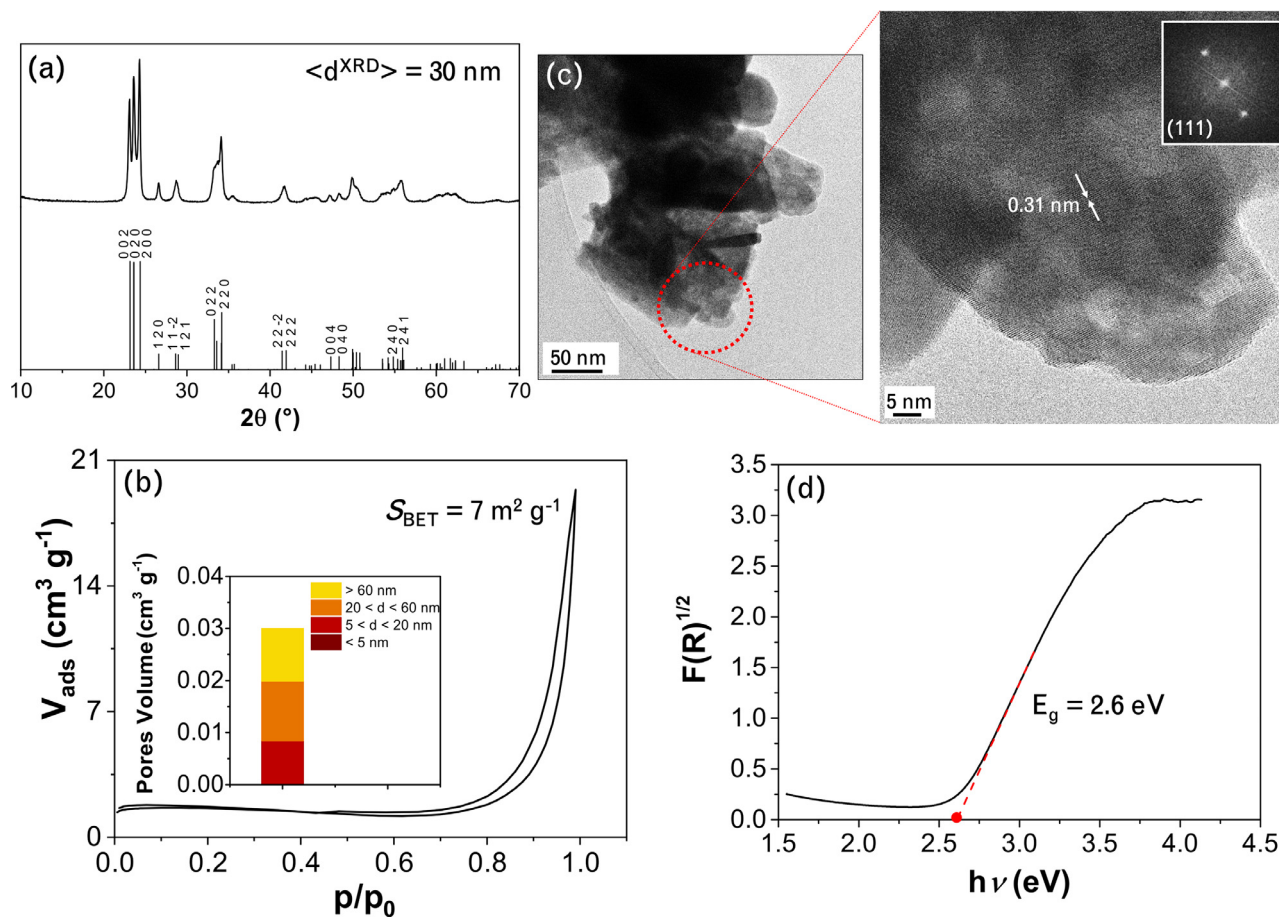
Fig. 1. (a) Comparison between XRD patterns of the as-synthesized and standard WO_3 γ−monoclinic polymorph in which the main peaks are indicated by the Miller's indexes (source: International Centre for Diffraction Data - ICDD n. 01-075-2072). (b) BET isotherm alongside with the pores distribution by BJH analysis and active surface area value. (c) HR-TEM images (inset: Fourier Transformation evidencing the (1 1 1) plane). (d) Optical band gap evaluation by Kubelka-Munk elaboration of the DRS spectrum.

4.3. Theoretical characterization of the active WO_3 surface

WO_3 surface was modeled by applying the $\begin{pmatrix} 1 & 1 \\ 1 & -1 \end{pmatrix}$ reconstruction, *i.e.* the most stable structure according to the literature [47]. This reconstruction can be obtained by removing half of the terminal O atoms exposed in the top layer. Since the W-O-W chains along the **c** axis are characterized by alternating long and short W-O bonds [41], we removed the terminal O atoms characterized by longer (hence weaker) W-O bonds. The same process was applied to the bottom layer. By doing so, no artificial mid-gap states appear in the electronic structure of the surface. The final slab used in our calculations is shown in Fig. 3(a): it has a thickness of six "WO_6" octahedra and includes a 18 Å vacuum layer to avoid spurious interactions between periodic replicas of the cell. The geometry of the first four layers has been optimized to take into account surface relaxation effects. The electron density distribution of the system has been analyzed within the framework of the Quantum Theory of Atoms in Molecules [57], using the Critic2 code [58].

The density of states (DOS) of the clean, non-defective surface, reported in Fig. 3(b), shows that it acts as an insulator with a calculated band gap amounting to 2.06 eV (to be compared with the calculated bulk value of 2.48 eV). The valence band is dominated by the 2p orbitals of the O atoms, while the d states of W atoms fill the conduction band. All the W atoms (both the

esacoordinated and the pentacoordinated ones) have an oxidation state very close to W^{6+}, as expected in a strongly ionic crystal.

4.3.1. With a bulk oxygen vacancy

Typical WO_3 samples are often sub-stoichiometric in oxygen [59], giving rise to a certain conductivity which drastically decreases when an oxidizing species such as molecular oxygen is pumped in the chamber. The crucial role of oxygen vacancies in standard WO_3 is commonly reported in literature and widely exploited in order to interpret the material electrical and magnetic behaviour, as well as its sensing properties [32,60]. In our simulations, this defect was reproduced by removing a neutral oxygen atom at the center of the slab, and relaxing the system again. In this case the density of oxygen vacancies amounts to 0.7% (one vacancy every 144 oxygen atoms). As expected, the two electrons left in the system cause a partial population of the conduction band, correctly reproducing the experimental electrical response (see Fig. 3c). The new empty state, due to the bulk vacancy and appearing just above the Fermi level (E_F), is mainly localized on the W atoms belonging to the chain extending along **c** (normal to the surface) and including the defect. The two extra electrons in the conduction band are delocalized and belong to the whole system. Differently, the surface state which appears at the top of the valence band in Fig. 3c is completely localized on the O atoms of the first layer of the slab. Due to the presence of this surface state, the band gap slightly decreases down to 1.9 eV. The electric
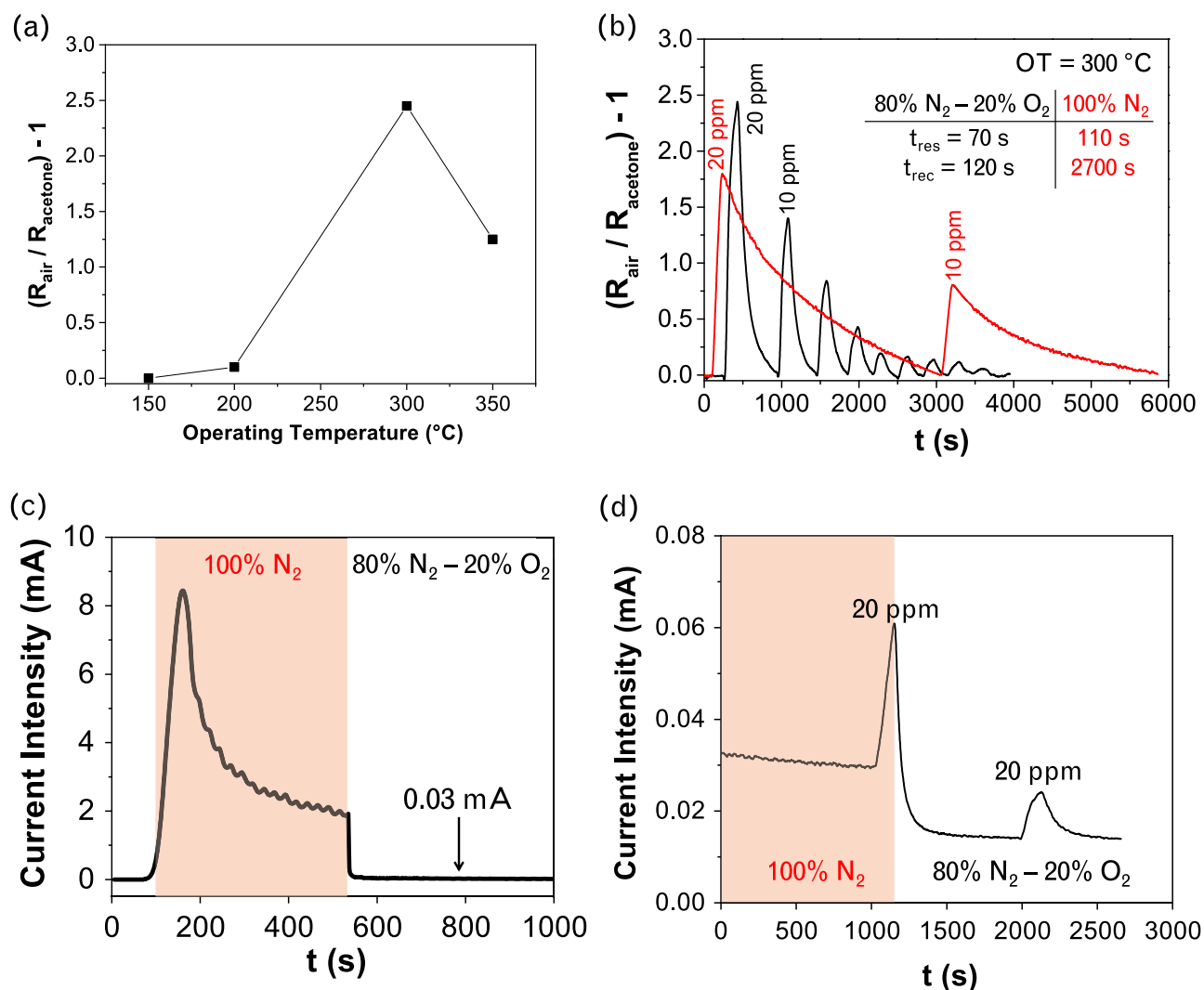
Fig. 2. (a) Signal response with the increasing of the Operating Temperature (OT) obtained towards 20 ppm of acetone. (b) In black: sensor response in simulated air 80% N_2 – 20% O_2 towards decreasing acetone concentrations. In red: sensor response in inert atmosphere (100% N_2). The table reports the respective average response (t_{res}) and recovery (t_{rec}) times showing very low standard deviations (<5%), denoting almost the same value for all the analyte concentrations. (c) Material current variation only by changing the gas carrier in the sensing chamber. After the first 80 s, the temperature is raised from RT to 300 °C. (d) Sensor response towards 20 ppm acetone when the atmosphere is changed from inert to simulated air.

dipole moment of this defective slab amounts to −0.67 a.u., reflecting an electron transfer towards the surface of 0.4 e^-, due to the surface state in the first layer. This defective slab (Surf in the following) is still non-magnetic, because of the very low vacancies concentration: the more complex configurations presented in the following will be discussed in relation to this reference system.

4.3.2. With both a bulk and a surface vacancy (Surf-O system)

It is known from the literature [17] that, while bulk oxygen defects mainly affect the conductivity, surface vacancies are a key component for the adsorption and transformation mechanisms on metal oxide surfaces, acting as particularly reactive sites for gas adsorption and molecular reactions [33]. When considering a surface with an additional oxygen vacancy in the first layer (Surf-O hereinafter, shown in Fig. 4e), the situation retrieved by our calculations changes significantly and the system becomes magnetic with a magnetic moment equal to 0.9 μ_B. The energy necessary to remove a couple of non-interacting O atoms from the surface and to form one O_2 molecule in gas phase amounts to 3.15 eV per atom. From a thermodynamic perspective, this means that an oxygen molecule prefers to dissociate in presence of defective surface,

leaving O atoms adsorbed on it. On the other hand, this behaviour was never observed on a stoichiometric surface. All terminal oxygen atoms, including those involved in the adsorption/desorption process, are electronically equivalent and bear a total charge of approximately 8 electrons. Hence, they can be classified as O^{2-}.

The density of states of the Surf-O system (see red line in Fig. 4a and b) shows four new sharp peaks around E_F, of which only one is occupied and corresponds to a majority state localized on the W atom just below the surface vacancy and weakly hybridized with the bulk vacancy state. The oxidation state of this tungsten becomes in this way W^{5+}. The analogue minority state is empty and the remaining two empty peaks in the conduction band are still localized on W atoms but without any hybridization. Three out of the four electrons in the conduction band are delocalized on the whole system and in particular on the surface layers. To sum up, when a terminal O^{2-} species detaches from the surface leaving a vacancy, it releases two electrons in the conduction band. One of them is delocalized on the whole system and adds up to the ones released by the bulk vacancy, contributing to the global conductivity, while the other one is localized on the W atom below and contributes to the surface reactivity. As a consequence, the electric
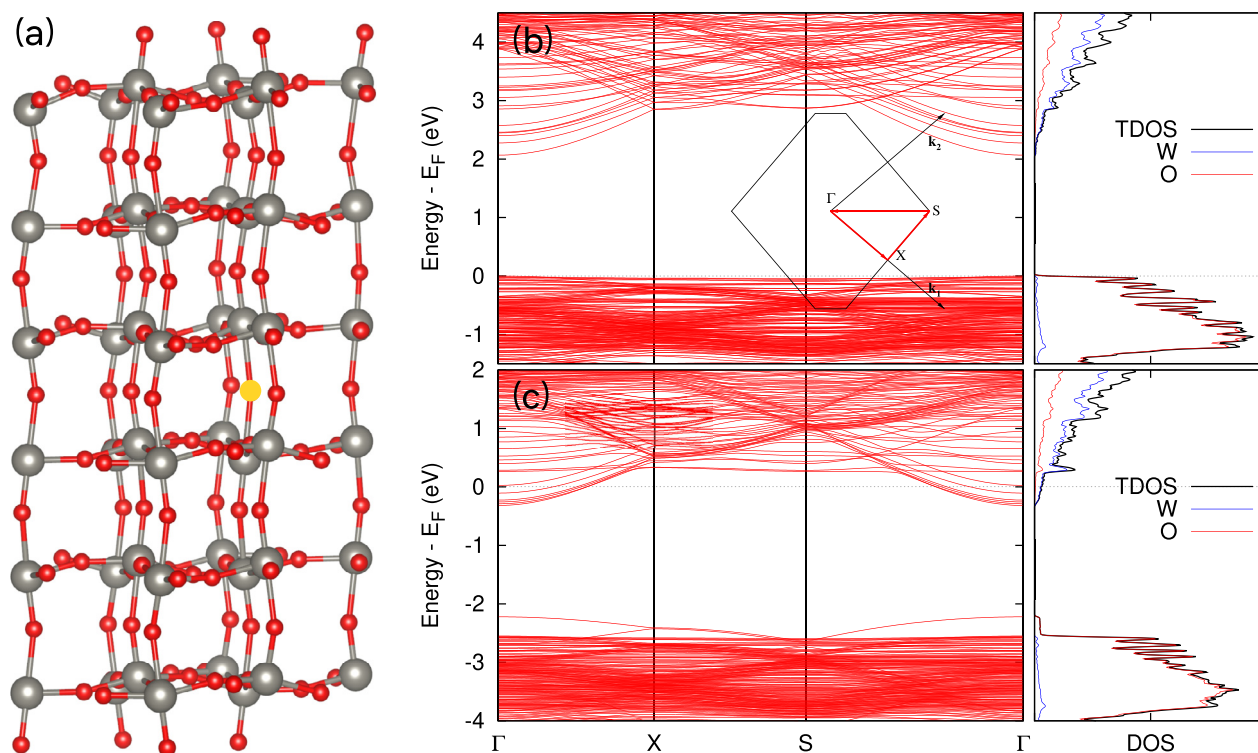
Fig. 3. (a) Structural model of the surface slab structure. The bulk O atom that was eventually removed in calculations has been coloured in yellow. Right panels: surface band structure and corresponding density of states, including projections over tungsten and oxygen atoms for (b) the clean surface and (c) in presence of a bulk vacancy. Panel (b) includes a representation of the surface Brillouin zone and an highlight of the path used for the band structure calculations.
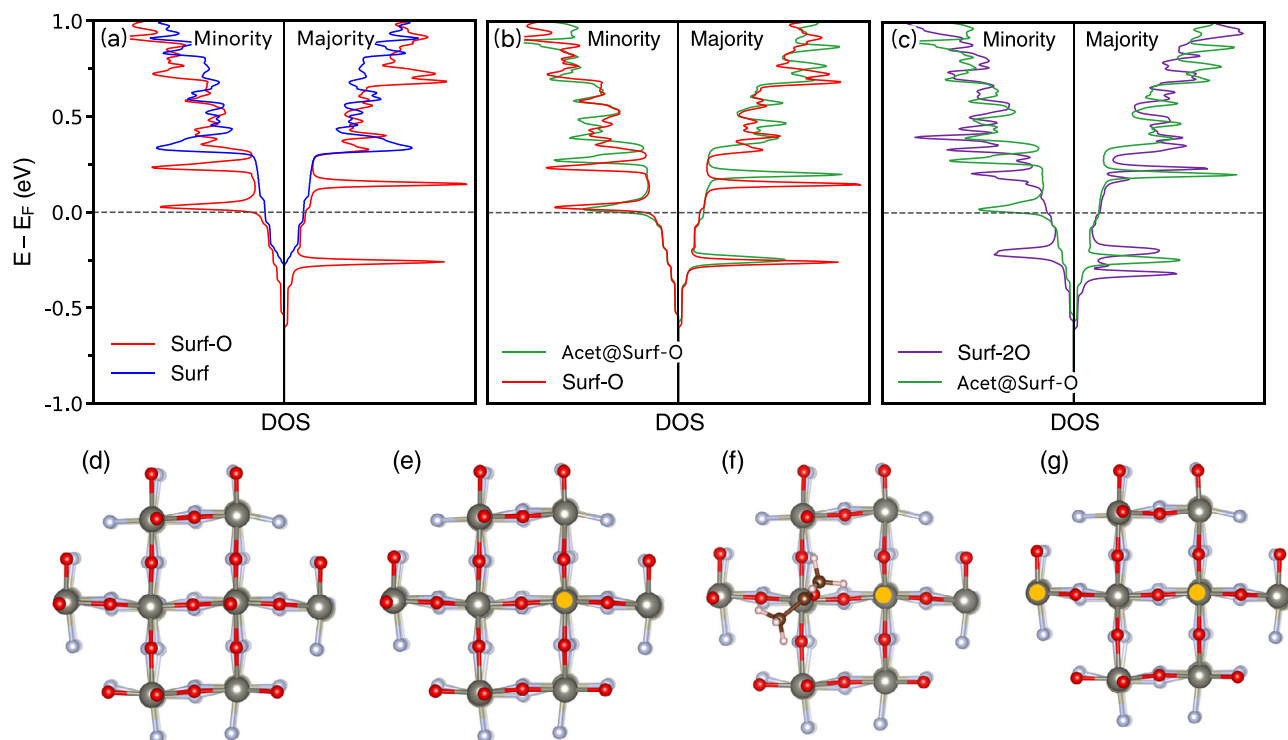
Fig. 4. (a) Comparison, focused on the portion of conduction band around the Fermi level, between the total DOS calculated for the WO_3 surface slab with a single surface oxygen vacancy (Surf-O, red line) and without surface oxygen vacancies (Surf, blue line). (b) DOS comparison between slabs with a single surface oxygen vacancy, in presence (Acet@Surf-O, green line) and in absence (Surf-O) of an adsorbed acetone molecule. (c) DOS comparison between the slab with a single surface oxygen vacancy in presence of an adsorbed acetone molecule (Acet@Surf-O) and the slab with two oxygen vacancies (Surf-2O, purple line). This case compares the system before and after acetone reaction with surface oxygen. (d-g): top views of the systems mentioned above: Surf, Surf-O, Acet@Surf-O, Surf-2O, respectively. Surface oxygen vacancies are highlighted by yellow dots. The bottom layers of the slabs are coloured with lighter colours for better visualization of the top layer.

dipole moment changes its sign and measures 2.08 a.u., due to the charge unbalance caused by the surface vacancy.

4.3.3. With a bulk and two surface vacancies (Surf-2O system)

As already highlighted, gas sensing is predominantly a surface-based phenomenon; hence, surface architecture and oxidation states are very significant factors that largely influence the sensor performance. In order to better explore this point, we also studied an even more defective surface, trying to detect the role of W atoms with modified oxidation states. This system, called Surf-2O and shown in Fig. 4g, has one bulk oxygen vacancy plus two surface ones, not contiguous. The energy involved in the desorption/adsorption process is almost equivalent to the previous case, *i.e.* the energy cost to remove the second oxygen is 3.23 eV. The DOS (see purple line in Fig. 4c) shows four peaks around the Fermi level, three of which are occupied while one is empty. The two occupied majority states are localized on the two W atoms just below the surface defects, while the minority occupied state is localized on just one of them. It follows that one of these W atoms has a 4+ oxidation state, which qualifies this site as the most reactive one. Notably, the presence of the second surface vacancy does not increase the number of electrons participating to the conduction, as the additional two released electrons are both localized on the W^{4+}. Consequently the magnetic moment of the system is still ca. 1 μ_B. In this configuration, the electric dipole moment further increases to 3.93 a.u. Remarkably, any increase in the number of surface vacancies is accompanied by a slight migration of conduction electrons from the bulk material towards the surface. This behaviour can be put in relation with the hypothesis, often advanced in literature [15,61], that adsorbed oxygen species may scatter conduction electrons away from the surface, determining the formation of a depletion layer which reduces the electron mobility and hence the MOS conductivity. The formation of surface vacancies acts in the opposite direction, leading to a larger active volume.

4.3.4. Acetone adsorption on Surf-O

Finally, in order to investigate the device response towards acetone gas, we have considered one acetone molecule interacting with a WO_3 slab of 190 atoms, including both a bulk and a surface oxygen vacancy (Acet@Surf-O, see Fig. 4f). The dipole moment qualifies the adsorption geometry with the carbonyl group of the acetone molecule pointing towards the surface as the most energetically stable. The oxygen atom of acetone directly interacts with one of the pentacoordinated W atoms of the first layer, with an W-O interatomic distance that spans from 2.11 to 2.24 Å, depending on the specific adsorption site. Accordingly, the binding energy ranges from 1.26 to 1.58 eV, reaching its highest value when the molecule is adsorbed on a vacancy site. A modest charge transfer of about one tenth of electrons from the acetone molecule to the sensor surface occurs in all configurations. The electric dipole moment of the acetone molecule in the gas phase amounts to 1.32 a.u. and sums up with that of the surface, resulting in a value of 6.19 a.u. for the global Acet@Surf-O system. The magnetic moment is still positive and equal to 0.76 μ_B. Looking at the DOS comparison reported in Fig. 4b, it can be seen that the electronic properties of this system do not change significantly with respect to the Surf-O slab. The localized state close to E_F is still ascribable to the W atom below the surface vacancy, whose oxidation state remains W^{5+}.

5. Discussion

The ionosorption model is rather popular in the literature and is often evoked in order to explain the sensing behaviour of WO_3 [32] and of several metal oxides, including for example SnO_2 [31] and ZnO [22]. The model considers many reactive steps

between acetone and surface oxygen species, eventually leading to complete oxidation to CO_2 and H_2O. Unfortunately, to the best of our knowledge, only a few studies [62–64] provide direct evidence of the evolution of the products of acetone oxidation upon MOS, and, among them, only few concerns WO_3 [33,64]. Sun et al. identified several acetone oxidation products on Mn_3AlO [62], while El-Mazaawi et al. reported CO_2 evolution from acetone on TiO_2 under UV irradiation [63]. The closest comparison with our specific case is provided by Li et al., which reported CO_2 evolution from acetaldehyde on WO_3 only by effect of thermal heating [65]. These considerations suggest that acetone oxidation on WO_3 surface is indeed possible, an hypothesis which is confirmed and strengthened by our DFT calculations which point out a reactivity enhancement of many surface sites upon oxygen exchange with the environment. At the same time, given the overall complexity of the scenario, other phenomena might play an important role in the sensing process alongside with reactions. This section follows the course of a typical sensing experiment, with the aim of identifying the physico-chemical processes determining the device response.

5.1. Sample stabilization at 300 °C

At the beginning of each sensing test, sample temperature is raised from RT to 300 °C, while keeping the chamber under inert atmosphere (100% N_2). The resulting current response, shown in Fig. 2c consists in a rapid increase, followed by a slower decrease until a plateau is reached. In a recent study by Yu et al. [66], where temperature programmed desorption analysis was performed on WO_3 samples, a desorption peak measured around 300-350 °C was attributed, among the possible oxygen-based adsorbates, to O_2^-. According to our calculations, however, oxygen can significantly affect the surface electronic properties only if adsorbed as O^{2-}. That being said, we cannot exclude that a more sophisticated modelization may lead to a larger variety of oxygen adsorbates. Whatever the nature of the desorbed species, the cited study provides experimental evidence that an electron attractor is removed from WO_3 surface at our operating temperature. Every time a chemically bound oxygen species leaves the surface, a vacancy is formed and some charge is released back to the conduction band (two electrons, in case of O^{2-}). Part of this charge is delocalized and can directly contribute to the material conductivity, justifying the initial current increase. The corresponding change in the material electronic structure is highlighted by the DOS comparison in Fig. 4a. The slow current decrease following the peak can be attributed to the saturation of the recently formed surface vacancies by temperature-promoted slow diffusion of lattice oxygen from the material bulk phase towards its surface, as already suggested by Li et al. [65]. The driving force of this process is the lower thermodynamic stability of surface vacancies with respect to bulk vacancies (0.51 eV). The result is a surface oxygen enrichment which, as previously discussed, leads to a less conductive state. Furthermore, as pointed out in Section 4.3, decreasing the number of surface vacancies determines the migration of conduction band electrons from the material surface towards the bulk phase, lowering in this way the sensor conductivity.

Overall, it can be reasonably assumed that temperature promotes three different processes on WO_3 and in general on metal oxide semiconductors: *i*) simple thermal promotion of electrons from defect states to the conduction band; *ii*) dissociation of W-O bonds resulting in formation of surface oxygen vacancies; *iii*) oxygen atom diffusion from the bulk phase towards the surface.

5.2. Oxygen introduction

As soon as O_2 is introduced into the sensing chamber, kept under inert atmosphere at high temperature, an abrupt current

decrease is observed (see Fig. 2c). According to the aforementioned DFT simulations, this behaviour can only be attributed to the saturation of surface oxygen vacancies by O_2, which dissociates into an oxygen atom directly bound to the surface and a free oxygen radical, which can either saturate another surface vacancy or be available for reactions. Each adsorbed O atom withdraws electrons from the conduction band, explaining the observed current decrease.

As a consequence, a net difference in baseline height is observed when comparing the sensor response in presence and in absence of gaseous oxygen, as shown in Fig. 2(d). In the former case, surface oxygen coverage is assumed to be higher due to the continuous replenishment of surface vacancies by the constant O_2 flow, thus determining lower baseline values. Conversely, in the latter case, the baseline current values are approximately two times higher. Indeed, in absence of O_2, the only possible vacancy saturation mechanism is lattice oxygen diffusion from the bulk material, which is a slow process and should reasonably determine a lower surface oxygen coverage at the equilibrium.

5.3. Acetone introduction

When acetone gas is introduced, a net current increase determines the sensor response. The origin of this behaviour can be ascribed to two different mechanisms: *i*) simple acetone adsorption as an electron donor; *ii*) acetone adsorption in presence of a reactive surface site followed by acetone oxidation, that leads to a net decrease of oxygen surface coverage.

These two mechanisms do not conflict and should produce the same rough experimental output, *i.e.* a current increase. They are both compatible with our experimental and theoretical observations, hence we cannot exclude their simultaneous occurrence. However, the specific experimental conditions may favour one process rather than the other, affecting the shape of the sensor response, *i.e.* the signal intensity, the response and recovery times.

In normal experimental conditions, the sample is exposed to gaseous oxygen, which enriches WO_3 surface of oxygen atoms (still leaving a not negligible amount of surface vacancies). When an acetone molecule adsorbs, it transfers to the sample ca. 0.1 electrons, according to our calculations. As stated in Section 4.3, surface vacancies can significantly alter the oxidation states of the tungsten atoms below, which could act as highly reactive adsorption sites for acetone oxidation. If an oxidation reaction occurs, each O atom transferred from the surface to the reaction products releases about 2 electrons back to the material, a fraction of whom can directly contribute to the system conductivity. Figure 4(b) can be seen as a qualitative comparison between the DOS structure before (Acet@Surf-O) and after (Surf-2O) the reaction, in which also a single O atom is removed from WO_3 surface. Nevertheless, proposing a specific reaction path would require a whole set of DFT and molecular dynamics calculations and it will not be discussed herein. Besides, as previously touched on, many experimental studies confirm the reactivity of MOS sensors towards organic molecules [62,67]. The oxygen transferred to the reaction products is continuously replaced by O_2, which can partially restore the surface oxygen concentration providing new fuel for subsequent reactions and/or release oxygen radicals which can eventually react in gas phase, promoting further oxidation steps. Surface oxygen vacancies formation (caused by reactions) and saturation (by O_2) reach an equilibrium whose position strictly depends on surface acetone concentration, hence on the total amount of acetone molecules present in the chamber. The net difference between surface oxygen coverage during this phase and the one prior to acetone exposure determines the peak height. Assuming that each reacting acetone molecule causes the detachment of at least one oxygen atom, in oxygen-rich atmosphere the contribution of reactions to the current increase can rapidly outweigh the one

deriving from simple acetone adsorption, since the charge transfer to the surface is much higher in the former process.

If O_2 is not present in the atmosphere, surface oxygen coverage prior to acetone introduction has to be significantly lower, compared to a situation in which surface vacancies can be rapidly replenished by surrounding O_2 molecules. Thus, adsorbed acetone molecules have much less oxygen fuel at their disposal in order to undergo oxidation reactions. On the other hand, the availability of free adsorption sites largely increases. As shown in Fig. 4(b), the effect of bare acetone adsorption on WO_3 electronic structure is almost negligible. The amount of charge transferred from an acetone molecule to WO_3 is small as well, compared to the charge released to the material whenever an oxygen atom is detached. Nevertheless, since acetone surface coverage is now much higher, the contribution of simple charge transfer to the total current change should increase, competing if not outweighing the contribution deriving from reactions. Moreover, the latter may prevail as soon as acetone is introduced and progressively lose importance, due to the rapidly consumption of the available oxygen atoms that cannot be readily replaced.

5.4. Acetone removal

When the analyte is purged out of the sensing chamber, two scenarios can be depicted depending on the experimental conditions: *i*) in *presence* of gaseous O_2, the pristine surface oxygen concentration is rapidly restored, determining the fast recovery times observed in Fig. 2(b); *ii*) in *absence* of gaseous O_2, unreacted acetone molecules can detach from the surface only by effect of thermal motion and, possibly, collisions with inert N_2 molecules. Each detached molecule removes a slight amount of charge from the WO_3 conduction band. The pristine surface oxygen concentration is restored by slow thermal diffusion from the bulk phase. The combination of these two phenomena determines much longer recovery times (about an hour), as Fig. 2(b) confirms.

6. Conclusions

Herein, a comprehensive study on the acetone sensing mechanism by *n*-type WO_3 chemiresistors was pursued on both experimental and theoretical points of view, in order to perceive the actual key role played by oxygen species. Since gas sensing is renowned to be a phenomenon occurring at the material surface, for the first time an accurate model of the real $\gamma-$monoclinic WO_3 structure (the main polymorph from the adopted template synthesis) was obtained by including both bulk and surface vacancies. We found that target acetone molecules, adsorbed pointing the oxygen of the carbonyl group towards one of the pentacoordinated surface W atoms, release about 0.1 electrons to the semiconductor surface. Hence, to give insight into the surface phenomenon, we experimentally performed sensing measurements both in absence and presence of molecular oxygen in the gas carrier. We firstly observed that the introduction of pure O_2 into the sensing chamber provokes a drastic increase of the WO_3 resistance, as confirmed by our DFT calculations for which oxygen can saturate the material surface vacancies withdrawing electrons from the conduction band. Besides, when acetone is added to the in-going flux, two different phenomena, *i.e.* the simple acetone adsorption or its oxidation reaction, can be favoured depending on the presence or not of the oxygen flux. Particularly, the adsorption of oxygen fills the material surface vacancies tipping the balance towards a more favorable acetone oxidation, resulting in a transfer of oxygen atoms from the surface to the reaction products with a considerable electrons release to the WO_3 conduction band. This leads to a material resistance decrease. On the other hand, the absence of oxygen may cause the simple acetone adsorption to prevail

over the oxidative reaction contribution. Then, once the acetone flux is stopped, the initial WO_3 conductivity is rapidly restored in the presence of oxygen carrier, whereas it takes longer in inert atmosphere, since the pristine surface oxygen concentration can be restored only by the slow thermal diffusion of lattice oxygen from the bulk phase. To the authors' best knowledge, a deeper understanding of the acetone sensing by WO_3 material has not been reported so far. Furthermore, the unraveling of the oxygen role can actually open up new scenarios for the engineering of novel nanomaterials with boosted sensing features.

Declaration of Competing Interest

The authors declare that they have no known competing financial interests or personal relationships that could have appeared to influence the work reported in this paper.

Credit authorship contribution statement

Stefano Americo: Formal analysis, Data curation, Writing - original draft. **Eleonora Pargoletti:** Conceptualization, Data curation, Writing - original draft. **Raffaella Soave:** Conceptualization, Formal analysis, Data curation, Writing - review & editing. **Fausto Cargnoni:** Conceptualization, Writing - review & editing. **Mario Italo Trioni:** Conceptualization, Formal analysis, Data curation, Writing - review & editing, Supervision. **Gian Luca Chiarello:** Conceptualization, Writing - review & editing. **Giuseppina Cerrato:** Formal analysis, Data curation, Writing - review & editing. **Giuseppe Cappelletti:** Conceptualization, Writing - review & editing, Supervision.

Acknowledgements

References

[1] A.T. Güntner, N.A. Sievi, S.J. Theodore, T. Gulich, M. Kohler, S.E. Pratsinis, Non-invasive body fat burn monitoring from exhaled acetone with Si-doped WO_3-sensing nanoparticles, Anal. Chem. 89 (19) (2017) 10578–10584, doi:10.1021/acs.analchem.7b02843.

[2] A.T. Güntner, S. Abegg, K. Königstein, P.A. Gerber, A. Schmidt-Trucksäss, S.E. Pratsinis, Breath sensors for health monitoring, ACS Sens. 4 (2) (2019) 268–280, doi:10.1021/acssensors.8b00937.

[3] Y.-H. Zhang, C.-Y. Liu, B.-B. Jiu, Y. Liu, F.-L. Gong, Facile synthesis of Pd-decorated ZnO nanoparticles for acetone sensors with enhanced performance, Res. Chem. Intermed. 44 (3) (2018) 1569–1578, doi:10.1007/s11164-017-3185-z.

[4] M. Righettoni, A. Tricoli, S. Gass, A. Schmid, A. Amann, S.E. Pratsinis, Breath acetone monitoring by portable Si:WO_3 gas sensors, Anal. Chim. Acta 738 (2012) 69–75, doi:10.1016/j.aca.2012.06.002.

[5] M. Righettoni, A. Tricoli, S.E. Pratsinis, Thermally stable, silica-doped ε-WO_3 for sensing of acetone in the human breath, Chem. Mater. 22 (10) (2010) 3152–3157, doi:10.1021/cm1001576.

[6] M. Righettoni, A. Tricoli, S.E. Pratsinis, Si:WO_3 sensors for highly selective detection of acetone for easy diagnosis of diabetes by breath analysis, Anal. Chem. 82 (9) (2010) 3581–3587, doi:10.1021/ac902695n.

[7] C.N. Tassopoulos, D. Barnett, T.R. Fraser, Breath-acetone and blood-sugar measurements in diabetes, Lancet 293 (7609) (1969) 1282–1286, doi:10.1016/s0140-6736(69)92222-3.

[8] M. Righettoni, A. Tricoli, Toward portable breath acetone analysis for diabetes detection, J. Breath. Res. 5 (3) (2011) 037109, doi:10.1088/1752-7155/5/3/037109.

[9] A. Tricoli, N. Nasiri, S. De, Wearable and miniaturized sensor technologies for personalized and preventive medicine, Adv. Funct. Mater. 27 (15) (2017) 1605271, doi:10.1002/adfm.201605271.

[10] A. Tricoli, G. Neri, Miniaturized bio-and chemical-sensors for point-of-care monitoring of chronic kidney diseases, Sensors 18 (4) (2018) 942, doi:10.3390/s18040942.

[11] H. Chen, R. Bo, A. Shrestha, B. Xin, N. Nasiri, J. Zhou, I. Di Bernardo, A. Dodd, M. Saunders, J. Lipton-Duffin, et al., NiO–ZnO Nanoheterojunction Networks for Room-Temperature Volatile Organic Compounds Sensing, Adv. Opt. Mater. 6 (22) (2018) 1800677, doi:10.1002/adom.201800677.

[12] H.W. Kim, Y.J. Kwon, A. Mirzaei, S.Y. Kang, M.S. Choi, J.H. Bang, S.S. Kim, Synthesis of zinc oxide semiconductors-graphene nanocomposites by microwave irradiation for application to gas sensors, Sens. Actuators B Chem. 249 (2017) 590–601, doi:10.1016/j.snb.2017.03.149.

[13] J. Lee, C. Lim, H. Park, H. Song, S. Choi, D. Lee, Zno-CuO core-hollow cube nanostructures for highly sensitive acetone gas sensors at the ppb level, ACS Appl. Mater. Interfaces 12 (2020) 35688–35697, doi:10.1021/acsami.0c08593.

[14] Q.-Q. Jia, H.-M. Ji, D.-H. Wang, X. Bai, X.-H. Sun, Z.-G. Jin, Exposed facets induced enhanced acetone selective sensing property of nanostructured tungsten oxide, J. Mater. Chem. A 2 (2014) 13602–13611, doi:10.1039/C4TA01930J.

[15] A. Tricoli, M. Righettoni, A. Teleki, Semiconductor gas sensors: dry synthesis and application, Angew. Chem. Int. Ed. 49 (42) (2010) 7632–7659, doi:10.1002/anie.200903801.

[16] J. Zhang, X. Liu, G. Neri, N. Pinna, Nanostructured Materials for Room-Temperature Gas Sensors, Adv. Mater. 28 (5) (2016) 795–831, doi:10.1002/adma.201503825.

[17] A.A. Abokifa, K. Haddad, J. Fortner, C.S. Lo, P. Biswas, Sensing mechanism of ethanol and acetone at room temperature by SnO_2 nano-columns synthesized by aerosol routes: theoretical calculations compared to experimental results, J. Mater. Chem. A 6 (5) (2018) 2053–2066, doi:10.1039/C7TA09535J.

[18] A.-K. Elger, C. Hess, Elucidating the mechanism of working SnO_2 gas sensors using combined operando UV/Vis, Raman, and IR spectroscopy, Angew. Chem. Int. Ed. 58 (42) (2019) 15057–15061, doi:10.1002/anie.201908871.

[19] F. Wang, C. Di Valentin, G. Pacchioni, DFT study of hydrogen adsorption on the monoclinic WO_3 (001) surface, J. Phys. Chem. C 116 (19) (2012) 10672–10679, doi:10.1021/jp302210y.

[20] L. Zhao, F.H. Tian, X. Wang, W. Zhao, A. Fu, Y. Shen, S. Chen, S. Yu, Mechanism of CO adsorption on hexagonal WO_3 (001) surface for gas sensing: A DFT study, Comput. Mater. Sci. 79 (2013) 691–697, doi:10.1016/j.commatsci.2013.07.046.

[21] Y. Chen, H. Qin, X. Wang, L. Li, J. Hu, Acetone sensing properties and mechanism of nano-$LaFeO_3$ thick-films, Sens. Actuators B Chem. 235 (2016) 56–66, doi:10.1016/j.snb.2016.05.059.

[22] P. Sahay, Zinc oxide thin film gas sensor for detection of acetone, J. Mater. Sci. 40 (16) (2005) 4383–4385, doi:10.1007/s10853-005-0738-0.

[23] K. Yuan, C.-Y. Wang, L.-Y. Zhu, Q. Cao, J.-H. Yang, X.-X. Li, W. Huang, Y.-Y. Wang, H.-L. Lu, D.W. Zhang, Fabrication of a micro-electromechanical system-based acetone gas sensor using CeO_2 nanodot-decorated WO_3 nanowires, ACS Appl. Mater. Interfaces 12 (2020) 14095–14104, doi:10.1021/acsami.9b18863.

[24] A. Gurlo, Interplay between O_2 and SnO_2: oxygen ionosorption and spectroscopic evidence for adsorbed oxygen, ChemPhysChem 7 (10) (2006) 2041–2052, doi:10.1002/cphc.200600292.

[25] R. Bo, N. Nasiri, H. Chen, D. Caputo, L. Fu, A. Tricoli, Low-voltage high-Performance UV photodetectors: an interplay between Grain Boundaries and Debye Length, ACS Appl. Mater. Interfaces 9 (3) (2017) 2606–2615, doi:10.1021/acsami.6b12321.

[26] N. Nasiri, D. Jin, A. Tricoli, Nanoarchitechtonics of visible-blind ultraviolet photodetector materials: critical features and nano-microfabrication, Adv. Opt. Mater. 7 (2) (2019) 1800580, doi:10.1002/adom.201800580.

[27] Z.Q. Zheng, J.D. Yao, B. Wang, G.W. Yang, Light-controlling, flexible and transparent ethanol gas sensor based on ZnO nanoparticles for wearable devices, Sci. Rep. 5 (1) (2015) 11070, doi:10.1038/srep11070.

[28] G. Lan, J. Nong, W. Jin, R. Zhu, P. Luo, H. Jiang, W. Wei, Enhanced UV photoresponse employing 3D graphene nanowalls/SnO_2 nanocomposite film, Surf. Coat. Technol. 359 (2019) 90–96, doi:10.1016/j.surfcoat.2018.12.052.

[29] S. Ardizzone, G. Cappelletti, C. Ricci, A. Sin, Nanocrystalline WO_3 polymorphs. Surfactant assisted growth steps to tailor microstructure and NO_2 response, J. Nanosci. Nanotechnol. 10 (12) (2010) 8367–8374, doi:10.1166/jnn.2010.2743.

[30] L. Saadi, C. Lambert-Mauriat, V. Oison, H. Ouali, R. Hayn, Mechanism of NO_x sensing on WO_3 surface: first principle calculations, Appl. Surf. Sci. 293 (2014) 76–79, doi:10.1016/j.apsusc.2013.12.095.

[31] J. Li, P. Tang, J. Zhang, Y. Feng, R. Luo, A. Chen, D. Li, Facile synthesis and acetone sensing performance of hierarchical SnO_2 hollow microspheres with controllable size and shell thickness, Ind. Eng. Chem. Res. 55 (12) (2016) 3588–3595, doi:10.1021/acs.iecr.6b00060.

[32] R.S. Khadayate, J.V. Sali, P.P. Patil, Acetone vapor sensing properties of screen printed WO_3 thick films, Talanta 72 (3) (2007) 1077–1081, doi:10.1016/j.talanta.2006.12.043.

[33] A. Staerz, S. Somacescu, M. Epifani, T. Kida, U. Weimar, N. Barsan, WO_3-based gas sensors: identifying inherent qualities and understanding the sensing mechanism, ACS Sensors 5 (2020) 1624–1633, doi:10.1021/acssensors.0c00113.

[34] Z. Qiu, Z. Hua, Y. Li, M. Wang, D. Huang, C. Tian, C. Zhang, X. Tian, E. Li, Acetone sensing properties and mechanism of Rh-loaded WO_3 nanosheets, Front. Chem. 6 (2018) 385, doi:10.3389/fchem.2018.00385.

[35] W. Kohn, L.J. Sham, Self-consistent equations including exchange and correlation effects, Phys. Rev. 140 (4A) (1965) A1133, doi:10.1103/PhysRev.140.A1133.

[36] E. Pargoletti, S. Verga, G.L. Chiarello, M. Longhi, G. Cerrato, A. Giordana, G. Cappelletti, Exploring $Sn_xTi_{1-x}O_2$ solid solutions grown onto graphene oxide (GO) as selective toluene gas sensors, Nanomaterials 10 (4) (2020) 761, doi:10.3390/nano10040761.

[37] E. Pargoletti, G. Cappelletti, Breakthroughs in the design of novel carbon-based metal oxides nanocomposites for VOCs gas sensing, Nanomaterials 10 (2020) 1485, doi:10.3390/nano10081485.

[38] E. Pargoletti, U.H. Hossain, I. Di Bernardo, H. Chen, T. Tran-Phu, G.L. Chiarello, J. Lipton-Duffin, V. Pifferi, A. Tricoli, G. Cappelletti, Engineering of SnO_2-graphene oxide nanoheterojunctions for selective room-temperature chemical sensing and optoelectronic devices, ACS Appl. Mater. Interfaces 12 (2020) 39549–39560, doi:10.1021/acsami.0c09178.

[39] E. Pargoletti, A. Tricoli, V. Pifferi, S. Orsini, M. Longhi, V. Guglielmi, G. Cerrato, L. Falciola, M. Derudi, G. Cappelletti, An electrochemical outlook upon the gaseous ethanol sensing by graphene oxide-SnO_2 hybrid materials, Appl. Surf. Sci. 483 (2019) 1081–1089, doi:10.1016/j.apsusc.2019.04.046.

[40] E. Pargoletti, U.H. Hossain, I. Di Bernardo, H. Chen, T. Tran-Phu, J. Lipton-Duffin, G. Cappelletti, A. Tricoli, Room-temperature photodetectors and voc sensors based on graphene oxidezno nano-heterojunctions, Nanoscale 11 (2019) 22932–22945, doi:10.1039/C9NR08901B.

[41] T. Vogt, P.M. Woodward, B.A. Hunter, The high-temperature phases of WO_3, J. Sol. State Chem. 144 (1) (1999) 209–215, doi:10.1006/jssc.1999.8173.

[42] C.J. Howard, V. Luca, K.S. Knight, High-temperature phase transitions in tungsten trioxide - the last word? J. Phys.: Condens. Matter 14 (3) (2002) 377–387, doi:10.1088/0953-8984/14/3/308.

[43] J.M. Soler, E. Artacho, J.D. Gale, A. García, J. Junquera, P. Ordejón, D. Sánchez-Portal, The SIESTA method for ab initio order-N materials simulation, J. Phys.: Condens. Matter 14 (11) (2002) 2745, doi:10.1088/0953-8984/14/11/302.

[44] J.P. Perdew, K. Burke, M. Ernzerhof, Generalized gradient approximation made simple, Phys. Rev. Lett. 77 (18) (1996) 3865, doi:10.1103/PhysRevLett.77.3865.

[45] N. Troullier, J.L. Martins, Efficient pseudopotentials for plane-wave calculations, Phys. Rev. B 43 (3) (1991) 1993, doi:10.1103/physrevb.43.1993.

[46] P. Rivero, V.M. García-Suárez, D. Pereñiguez, K. Utt, Y. Yang, L. Bellaiche, K. Park, J. Ferrer, S. Barraza-Lopez, Systematic pseudopotentials from reference eigenvalue sets for DFT calculations, Comput. Mater. Sci. 98 (2015) 372–389, doi:10.1016/j.commatsci.2014.11.026.

[47] C. Lambert-Mauriat, V. Oison, Density-functional study of oxygen vacancies in monoclinic tungsten oxide, J. Phys.: Condens. Matter 18 (31) (2006) 7361, doi:10.1088/0953-8984/18/31/028.

[48] L.G. Ferreira, M. Marques, L.K. Teles, Approximation to density functional theory for the calculation of band gaps of semiconductors, Phys. Rev. B 78 (12) (2008) 125116, doi:10.1103/PhysRevB.78.125116.

[49] L.G. Ferreira, M. Marques, L.K. Teles, Slater half-occupation technique revisited: the LDA-1/2 and GGA-1/2 approaches for atomic ionization energies and band gaps in semiconductors, AIP Adv. 1 (3) (2011) 032119, doi:10.1063/1.3624562.

[50] F.P. Koffyberg, K. Dwight, A. Wold, Interband transitions of semiconducting oxides determined from photoelectrolysis spectra, Solid State Comm. 30 (1979) 433–437, doi:10.1016/0038-1098(79)91182-7.

[51] K. Miyake, H. Kaneko, M. Sano, N. Suedomi, Physical and electrochromic properties of the amorphous and crystalline tungsten oxide thick films prepared under reducing atmosphere, J. Appl. Phys. 55 (7) (1984) 2747–2753, doi:10.1063/1.333280.

[52] P.P. González-Borrero, F. Sato, A.N. Medina, M.L. Baesso, A.C. Bento, G. Baldissera, C. Persson, G.A. Niklasson, C.G. Granqvist, A. Ferreira da Silva, Optical band-gap determination of nanostructured WO_3 film, Appl. Phys. Lett. 96 (6) (2010) 061909, doi:10.1063/1.3313945.

[53] P. Periasamy, T. Krishnakumar, M. Sathish, M. Chavali, P.F. Siril, V.P. Devarajan, Structural and electrochemical studies of tungsten oxide (WO_3) nanostructures prepared by microwave assisted wet-chemical technique for supercapacitor, J. Mater. Sci. Mater. Electron. 29 (8) (2018) 6157–6166, doi:10.1007/s10854-018-8590-6.

[54] H. Chen, R. Bo, T. Tran-Phu, G. Liu, A. Tricoli, One-Step Rapid and Scalable Flame Synthesis of Efficient WO_3 Photoanodes for Water Splitting, ChemPlusChem 83 (7) (2018) 569–576, doi:10.1002/cplu.201800061.

[55] N.M.G. Parreira, T. Polcar, A. Cavaleiro, Thermal stability of reactive sputtered tungsten oxide coatings, Surf. Coat. Technol. 201 (16) (2007) 7076–7082, doi:10.1016/j.surfcoat.2007.01.019.

[56] M. Esmaeili, G. Kiani, F. Shahriari Nogorani, S. Boroomand, Acetone sensing properties of hierarchical WO_3 core-shell microspheres in comparison with commercial nanoparticles, Int. J. Nano Dimens. 7 (3) (2016) 254–262, doi:10.7508/ijnd.2016.03.009.

[57] R.F.W. Bader, Atoms in Molecules: A Quantum Theory, International Series of Monographs on Chemistry, 22, Oxford University Press, Oxford (UK), 1990.

[58] A. Otero-de-la Roza, E.R. Johnson and, V. Luaña, Critic2: A program for real-space analysis of quantum chemical interactions in solids, Comput. Phys. Commun. 185 (2014) 1007, doi:10.1016/j.cpc.2013.10.026.

[59] S. Corby, L. Francàs, A. Kafizas, J.R. Durrant, Determining the role of oxygen vacancies in the photocatalytic performance of WO_3 for water oxidation, Chem. Sci. 11 (2020) 2907–2914, doi:10.1039/C9SC06325K.

[60] P. Kaur, S. Kaur, D. Arora, K. Asokan, D.P. Singh, et al., Influence of defect structure on colour tunability and magneto optical behaviour of WO_3 nanoforms, RSC Adv. 9 (36) (2019) 20536–20548, doi:10.1039/C9RA01901D.

[61] A. Mirzaei, S.G. Leonardi, G. Neri, Detection of hazardous volatile organic compounds (VOCs) by metal oxide nanostructures-based gas sensors: A review, Ceram. Int. 42 (14) (2016) 15119–15141, doi:10.1016/j.ceramint.2016.06.145.

[62] Y. Sun, X. Zhang, N. Li, X. Xing, H. Yang, F. Zhang, J. Cheng, Z. Zhang, Z. Hao, Surface properties enhanced Mn_xAlO oxide catalysts derived from Mn_xAl layered double hydroxides for acetone catalytic oxidation at low temperature, Appl. Catal. B 251 (2019) 295–304, doi:10.1016/j.apcatb.2019.03.035.

[63] M. El-Maazawi, A. Finken, A. Nair, V. Grassian, Adsorption and photocatalytic oxidation of acetone on TiO_2: an in situ transmission FT-IR study, J. Catal. 191 (1) (2000) 138–146, doi:10.1006/jcat.1999.2794.

[64] J. Lu, C. Xu, L. Cheng, N. Jia, J. Huang, C. Li, Acetone sensor based on WO_3 nanocrystallines with oxygen defects for low concentration detection, Mater. Sci. Semicond. Process. 101 (2019) 214–222, doi:10.1016/j.mssp.2019.05.038.

[65] Y. Li, C. Wang, H. Zheng, F. Wan, F. Yu, X. Zhang, Y. Liu, Surface oxygen vacancies on WO_3 contributed to enhanced photothermo-synergistic effect, Appl. Surf. Sci. 391 (2017) 654–661, doi:10.1016/j.apsusc.2016.07.042.

[66] W. Yu, Z. Shen, F. Peng, Y. Lu, M. Ge, X. Fu, Y. Sun, X. Chen, N. Dai, Improving gas sensing performance by oxygen vacancies in sub-stoichiometric WO_{3-x}, RSC Adv. 9 (14) (2019) 7723–7728, doi:10.1039/C9RA00116F.

[67] S. Morandi, A. Fioravanti, G. Cerrato, S. Lettieri, M. Sacerdoti, M.C. Carotta, Facile synthesis of ZnO nano-structures: morphology influence on electronic properties, Sens. Actuators B Chem. 249 (2017) 581–589, doi:10.1016/j.snb.2017.03.114.